

tion, we obtain an abundance of $12 + \log(\text{Cr}^+/\text{H}^+) = 4.28 \pm 0.03$. By comparing this value with the Fe^+ and Ni^+ abundances, we obtain $\log(\text{Cr}^+/\text{Ni}^+) = -0.61 \pm 0.05$ and $\log(\text{Cr}^+/\text{Fe}^+) = -1.88 \pm 0.07$, in agreement with the solar values of $\log(\text{Cr}/\text{Ni})_\odot = -0.57 \pm 0.05$ and $\log(\text{Cr}/\text{Fe})_\odot = -1.82 \pm 0.04$, respectively (Lodders 2019). Nevertheless, the spatial distribution of the Cr^+/Ni^+ and Cr^+/Fe^+ ratios along the HH 204 jet is not completely constant, as it is described in Sec. 5.2, which may be indicative of different ionization/depletion patterns between these elements. Unfortunately, although several [Cr III] lines are detected, we can not derive the Cr^{2+} abundance due to the lack of atomic data for this ion.

In the case of the Ca^+ abundance, we base our estimations in the [Ca II] $\lambda 7324$ line since $\lambda 7291$ is affected by a telluric absorption in our observations. Due to its low ionization potential, smaller than that of hydrogen, and owing to the presence of an ionization front in HH 204 (Núñez-Díaz et al. 2012), the resulting abundance may not represent the real gaseous Ca^+ abundance in the photoionized gas of HH 204.

4.5. Ionic abundances based on RLs

For the nebular component, the He^+ abundance is derived using $T_e(\text{high})$ and the lines considered in Table D14 of Paper I, which are the least affected by the metastability of the 2^3S level. However, we have used $T_e(\text{low})$ for HH 204. In this component, our determination of $T_e(\text{He I})$ is more consistent with $T_e(\text{low})$. This is because in HH 204, [O III] emission arises from a small localized area of higher ionized gas and $T_e([\text{O III}])$ may be not representative of the He^+ volume, as we describe in Sec. 5.1.

$\text{C II } \lambda 4267$ is partially blended in the two velocity components of cut 1 and therefore we base our calculations on $\text{C II } \lambda 9903$. We use $\text{C II } \lambda 4267$ in cut 2. C^{2+} abundance estimations based on both lines are in complete agreement in cut 2. Due to the similar ionization potentials of C^+ and He^0 and the considerations outlined in the previous paragraph, $T_e(\text{low})$ is also used for determining the C^{2+} abundance in HH 204.

Contrary to the situation presented in Paper I, in HH 204, O I RLs from multiplet 1 are severely affected by telluric emission features with the exception of $\text{O I } \lambda 7772$. We derive the O^+ abundance of the HH object using the intensity of this line and the predicted line strengths from Wiese et al. (1996) following Eq. 2 of Esteban et al. (1998).

Estimations of the O^{2+} abundance from RLs are based on the available O II lines of multiplet 1. These are not detected in the case of HH 204 (see Fig. 5). We use an

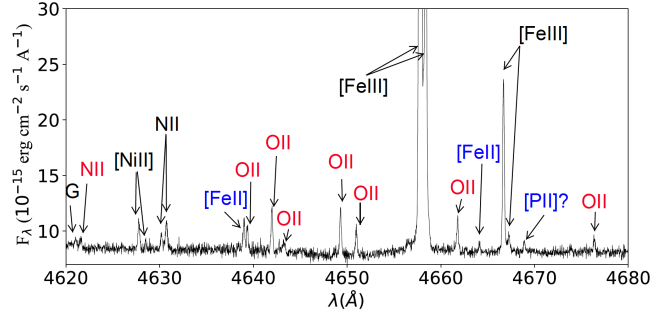


Figure 5: Section of the spectrum of the spatial cut 1 covering the spectral range 4620–4680 Å. Lines emitted exclusively by HH 204 are marked in blue, while those of the Orion Nebula are marked in red. The lines observed in both components are highlighted in black. Several O II RLs from multiplet 1 are present in the nebular component, but they are not observed in HH 204 due to its low ionization potential. The emission marked with a G is a ghost feature.

estimate of the upper limit of the intensity of $\lambda 4649$ line for this component.

5. UNVEILING HH 204

As it was mentioned in Sec. 3 we measure several lines pixel by pixel throughout the spatial coverage of HH 204. The spatial resolution in the blue and red arms of UVES is slightly different ($0.246''/\text{pixel}$ and $0.182''/\text{pixel}$ respectively). Cut 1 includes 30 pixels in the blue arm and 42 in the red one. In the pixel by pixel measurements, renormalization between lines in common in each arm is not enough to dilute possible differences in the integrated flux. However, $\text{H}\beta$ is observed in the spectra of both arms and therefore we split our pixel-spectra in two parts, 27 blue-pixel-spectra and 37 red-pixel-spectra, both groups normalized with respect to $f(\text{H}\beta)$. The missing first pixels (from east to west) of cut 1 of both arms were not included since the emission of HH 204 was too faint. We proceeded as follows: based on the $[\text{Fe III}] \lambda 4658/\lambda 4702$ line ratios we derive n_e along HH 204 in the blue arm. Once the density distribution was estimated, the calculation of $T_e([\text{O III}])$ was done, also in the blue arm through the $[\text{O III}] \lambda 4363/\lambda 4959$ line ratio. The spatial distribution of n_e was linearly interpolated in the red arm to estimate $T_e([\text{S III}])$ and $T_e([\text{N II}])$. Once the physical conditions are determined, we estimate the ionic abundances using the same procedure followed in Sec. 4.2. The zero point of the spatial distribution is located at coordinates: RA(J2000)= $05^{\text{h}}35^{\text{m}}22^{\text{s}}.81$, DEC(J2000)= $-05^{\circ}25'21.86''$, just at the apparent eastern – external – edge of the bowshock. To estimate the distance from the bowshock along the jet, we adopt an

↑ Need to make clear what velocity range is being integrated over.

Table 4: Chemical abundances obtained with CEL's of the integrated spectra of each component.

Ion	Cut 1		Cut 2	
	HH 204	Nebula + DBL	DBL	Nebula
O ⁺	8.62 ± 0.05	8.14 ± 0.05	8.26 ^{+0.13} _{-0.09}	8.18 ^{+0.06} _{-0.05}
O ²⁺	6.34 ± 0.02	7.96 ± 0.02	7.33 ^{+0.15} _{-0.10}	8.04 ± 0.02
N ⁺	7.72 ± 0.03	7.34 ± 0.03	7.40 ^{+0.08} _{-0.06}	7.29 ^{+0.04} _{-0.03}
Ne ²⁺	5.05 ± 0.03	7.16 ± 0.02	-	7.23 ^{+0.03} _{-0.02}
S ⁺	6.60 ± 0.04	5.93 ± 0.03	5.92 ^{+0.07} _{-0.06}	5.86 ^{+0.04} _{-0.03}
S ²⁺	6.80 ± 0.03	6.84 ± 0.03	6.85 ^{+0.10} _{-0.08}	6.89 ± 0.04
Cl ⁺	4.72 ± 0.03	4.17 ± 0.03	4.08 ^{+0.10} _{-0.09}	4.05 ± 0.04
Cl ²⁺	4.77 ^{+0.04} _{-0.03}	4.93 ± 0.04	4.99 ^{+0.16} _{-0.12}	4.98 ^{+0.06} _{-0.05}
Ar ²⁺	5.66 ± 0.03	6.10 ± 0.02	5.99 ^{+0.10} _{-0.08}	6.12 ± 0.02
Ar ³⁺	-	3.64 ^{+0.13} _{-0.12}	-	-
Fe ⁺	6.16 ± 0.04	-	-	4.72 ± 0.08
Fe ²⁺	6.49 ± 0.02	5.72 ± 0.04	5.56 ^{+0.10} _{-0.08}	5.77 ± 0.04
Fe ³⁺	< 5.11	5.73 ± 0.13	-	-
Ni ⁺	4.89 ± 0.02	-	-	-
Ni ²⁺	5.13 ± 0.03	4.37 ± 0.09	-	-
Ca ⁺	3.50 ± 0.03	-	-	-
Cr ⁺	4.28 ± 0.03	-	-	-

NOTE—Abundances in units of $12 + \log(X^{n+}/H^+)$.

Table 5: Chemical abundances obtained with RL's of the integrated spectra of each component.

Ion	Cut 1		Cut 2	
	HH 204	Nebula + DBL	DBL	Nebula
He ⁺	10.53 ± 0.02	10.85 ± 0.03	10.66 ± 0.06	10.92 ± 0.04
O ⁺	8.57 ± 0.03	-	-	-
O ²⁺	< 7.54	8.25 ± 0.06	-	8.40 ± 0.03
C ²⁺	7.76 ± 0.07	8.22 ± 0.04	-	8.37 ± 0.02

NOTE—Abundances in units of $12 + \log(X^{n+}/H^+)$.

heliocentric distance of 410 ± 10 pc (Binder & Povich 2018) to the Orion Nebula, based on *Gaia* DR2 parallaxes (Gaia Collaboration et al. 2018).

5.1. Small scale physical conditions

The resulting pixel by pixel distribution of physical conditions is shown in Fig. 6. We can see that $n_e([Fe\,III])$ increases as one approaches the shock front up to a factor of about 2, compared to the values at ~ 13 mpc from the bowshock. The distribution of $T_e([N\,II])$ is practically constant, while $T_e([S\,III])$ decreases slightly as

we approach the edge of the bowshock. Conversely, $T_e([O\,III])$ strongly increases when one approaches the bowshock.

The interpretation of the spatial distribution of $T_e([O\,III])$ is complex. In the presence of a shock, a photoionized gas can be heated at a temperature higher than that fixed by photoionization equilibrium (Zel'dovich & Raizer 1967) (see Sec. 11 of Paper I). After the shock passage, the gas cools down by radiative emission until reaching equilibrium temperature, forming a cooling zone whose extension will be inversely pro-

I would recommend a more neutral and less "causal" language.
It gives the impression that the [FeIII] emitting gas is approaching the bow shock,
which is probably not true.

Shouldn't this
be better in
the discussion
part?
Maybe best to
stick to
empirical description
here

This paragraph I am broadly in agreement with, apart from some details, but I still think that maybe it would be better not to mix discussion with the empirical description.

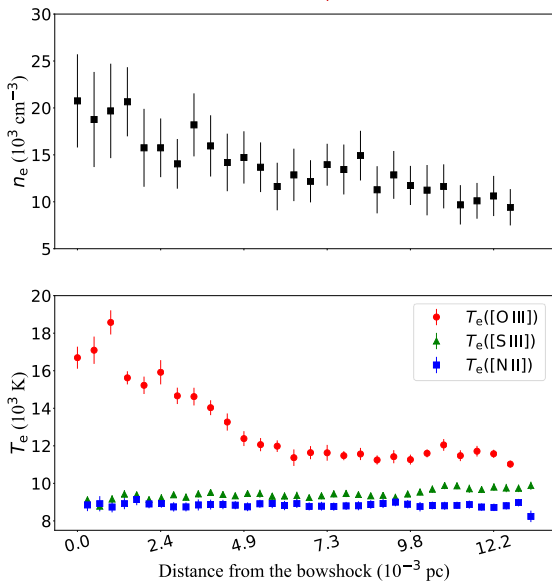


Figure 6: Spatial distribution of physical conditions as a function of the distance to the eastern – external – edge of the bowshock of HH 204. *Upper panel:* n_e ([Fe III]). The gas compresses as it approaches to the shock front, increasing its density. *Bottom panel:* T_e estimates with 3 diagnostics. While T_e ([S III]) and T_e ([N II]) remain unaltered, T_e ([O III]) shows a strong increase when approaching the shock.

I don't understand what is meant by entrainment here

portional to the electron density (Hartigan et al. 1987). If we assume that the high- T_e ([O III]) area corresponds to the cooling zone formed after the shock, the fact that T_e ([S III]) and T_e ([N II]) are not affected in the same way, would suggest that the high-ionization degree gas should have a much lower density than the low and medium-ionization degree gas and that both components coexist in HH 204. Although there is evidence of entrainment of material emitting in [O III] CELs feeding HH 204 (see Sec. 8), panels (a) and (b) from Fig. 2 show that the spatial and spectral distribution of [O III] and [O II] do not differ considerably. This fact can indicate two situations, or that there is no gas with two different physical conditions or, on the contrary, both components are intertwined in such a way that our UVES observations cannot separate them.

On the other hand, the kinetic energy of the electrons moving at a velocity $\sim 100 \text{ km s}^{-1}$ relative to the rest frame –as is the case for HH 204– is $\sim 51.8 \text{ eV}$ which is able to ionize an O^+ ion at rest into O^{2+} and excite it to its higher levels. In the bowshock, the difference in velocity between the “target” and the “projectile” gas is

I don't agree with this, unless you are talking about only the jet component. The [O III] lines also show a bow shock component, which is very different.

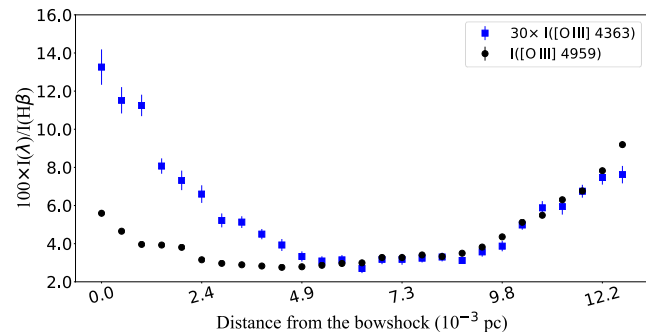


Figure 7: Same as Fig. 6 for the intensities of the [O III] $\lambda\lambda 4363, 4959$ lines. Line intensity ratios with respect to $H(\beta)$ have been normalized for a clearer comparison.

maximum, and so it would be the shock-ionization and excitation rates to the 1S_0 level of O^{2+} . This would create a localized high- T_e ([O III]) zone where temperature would decrease as we move away from the bowshock.

Therefore, we suggest that we are seeing the superposition of two different emission components: one from the bow shock and one from the Mach disk (the shock internal to the jet). The jet shock will have a lower Mach number, \mathcal{M} , than the bow shock so long as the unshocked jet is denser than the ambient medium, as appears to be the case in HH 204. The thickness of the equilibrium (cooled) shocked shell is proportional to \mathcal{M}^{-1} and so should be larger for the shell behind the Mach disk, which thus dominates the emission in much of the slit (displacements 5 to 12 mpc in Fig. 7). At smaller displacements, the contribution of the bow shock (from collisional heating) gets progressively larger, thus explaining the increase in T_e ([O III]). The expected length scale for this variation is roughly the radius of curvature of the bow shock, which agrees with the observed 5 mpc. The only reason that this effect is visible at all is that [O III] emission from the equilibrium shell is so weak. For lower ionization lines, the contribution of the bow shock to the total brightness is always negligible, even for positions close to the shock.

The fact that between 5 to 12 mpc in Fig. 6, T_e ([O III]) reaches an apparent equilibrium at a higher temperature than T_e ([N II]), may be due to the shock contribution of the wings, which are not perpendicular to the direction of propagation of HH 204.

Again: discussion

Although part of the aforementioned high-ionization degree gas may be out of photoionization equilibrium, fortunately, its impact is negligible in the global abundance analysis of HH 204. Considering the ionization fraction $O^{2+}/(O^+ + O^{2+}) = 0.005 \pm 0.001$ (see Table 4) – which would increase to $O^{2+}/(O^+ + O^{2+}) = 0.017 \pm 0.003$ if we determine the O^{2+} abundance using T_e ([N II]) – we infer that the contribution of the O^{2+} from the high-

Various problems here:

1. Electron have negligible mass compared with ions, so their KE is not relevant!
2. Cooling length is much shorter than could be resolved
3. To “discuss” – like

ionization degree gas is around $\sim 1\%$ of the oxygen abundance. A similar result is found for other metals. For example, by considering the solar Ne/O ratio recommended by Lodders (2019) and the Ne^{2+}/O value of HH 204, we estimate that $\text{Ne}^{2+}/\text{Ne} \sim 0.001$. The fact that $T_e([\text{N II}])$ and $T_e([\text{S III}])$ are kept in balance in HH 204 along the observed pixels proves that the low and medium-ionization degree gas, which comprises more than $\sim 99\%$ of the total, is in photoionization equilibrium.

5.2. Small-scale patterns in the ionic abundances

Fig. 8 shows the spatial distribution of the ionic abundances of O. As described in Sec. 5.1, the increase of $T_e([\text{O III}])$ may be related to shock heating. Therefore, we highlight in red the O^{2+} abundances in this area in the bottom panel of Fig. 8. In the upper panel, we show the O^+ abundances along all the distance range and the O ones in the area where $T_e([\text{O III}])$ remains constant. This panel shows that practically all O is in O^+ form. It should be noted that an increase of a factor of ~ 2 in the O^{2+} abundance would represent less than 1% of the total O, well below the associated uncertainties and, therefore, this increase would be undetected in analyses lacking our spatial and spectral resolutions.

In tables 4 and 5 we can see that the O^+ abundances determined from CELs and RLs for HH 204 are the same within the errors, so we do not find an abundance discrepancy (AD) for this ion, contrary to the situation found in practically all photoionized nebulae. Fig. 9 indicates the absence of any significant AD in all the observed areas of HH 204. Although some fluctuations seem to be present, they are very small in any case. The origin of the AD problem has been related to temperature, density or chemical inhomogeneities in the nebulae or fluorescence effects on the intensity of RLs (and references therein Peimbert 1967; Torres-Peimbert et al. 1980; Liu et al. 2001; Pequignot et al. 1991; García-Rojas & Esteban 2007; Escalante et al. 2012). In relation to this, there are three properties of HH 204 that we want to highlight: (i) In Sec. 5.1, we show that the spatial distribution of $T_e([\text{N II}])$ is constant, i. e. there are no significant temperature fluctuations in the plane of the sky that may be translated into fluctuations in the line of sight. The presence of temperature fluctuations would produce the underestimation of the O^+ abundance based on CELs. (ii) In Sec. 4.3, we show that the effects of starlight fluorescence are negligible in the determination of the abundances of Ni^+ and Fe^+ due to the large distance between HH 204 and the ionizing source in addition to the high density of the HH object. Thus, if there is any mechanism in which the contin-

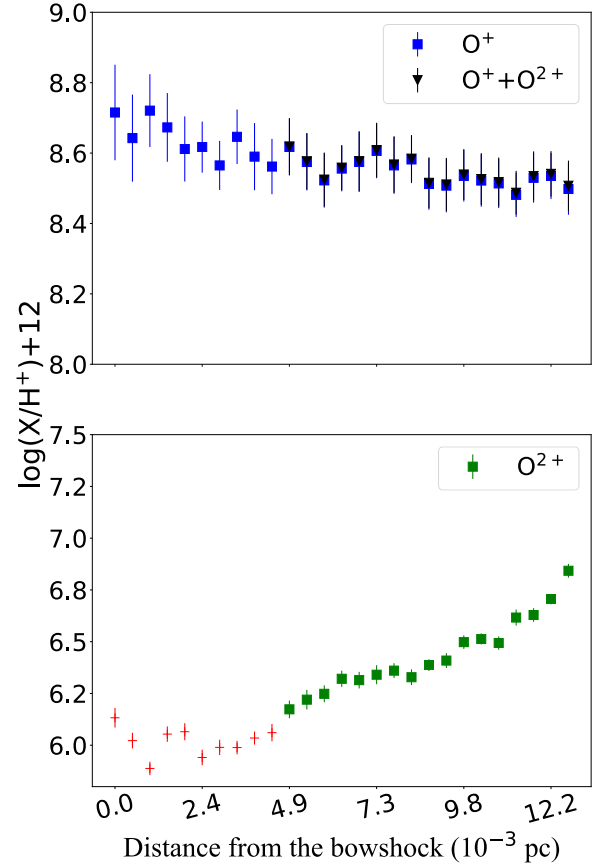


Figure 8: Same as Fig. 6 for ionic and total abundances of O. *Upper panel:* O^+ and total O abundances. The total abundance of O was calculated as the sum of O^+ and O^{2+} in the area where $T_e([\text{O III}])$ remains constant – distances between 4.9 and 13 mpc from the bowshock –. The contribution of O^{2+} to total O abundance is negligible compared to the abundance of O^+ . *Bottom panel:* O^{2+} abundances. The red crosses show the zone clearly affected by the shock (see Fig. 6, Fig. 7 and Sec. 5.1). The green squares indicate the area where $T_e([\text{O III}])$ remains constant.

uum pumping can affect the population of the levels of multiplet 1 of O I, this may be diminished in a similar way. Moreover, (Mesa-Delgado et al. 2009) report an $\text{ADF}(\text{O}^+) \sim 0$ in HH 202 S, which is located closer to the ionization source of the nebula, indicating that, in any case, O I lines of multiplet 1 are not likely to be exposed to fluorescence effects due to continuum pumping. (iii) The jet-geometry of HH 204, with a relatively small angle of $32 \pm 6^\circ$ with respect to the plane of the sky (see

The change in distance is negligible, so shouldn't affect the ionization parameter. I don't think the density increase is enough to explain the ionization change, so there must be an opacity effect, right?

MÉNDEZ-DELGADO ET AL.

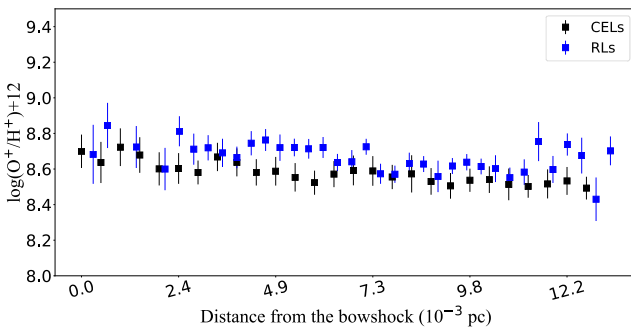


Figure 9: Same as Fig. 6 for O⁺ abundances determined with CELs and RLs.

Sec. 8), implies that any gradient in the physical conditions along the jet axis should be separated in the plane of the sky. This is a more favorable geometry for analysis than the case of a jet flowing directly towards the observer where different zones will overlap the same line of sight. Therefore, the existence of chemical or density inhomogeneities in the line of sight should not be significant. These three facts favor that the AD(O⁺) is small in HH 204. Unfortunately, we can not perform a similar analysis for the AD(O²⁺) because we do not detect O II RLs in HH 204.

In Fig. 10 we present the ionic abundances of Cl and S. The species of the same ionic charge of both elements show similar pixel by pixel distributions. The variations of S²⁺/H⁺ and Cl²⁺/H⁺ ratios along HH 204 are comparatively much smaller than those of S⁺/H⁺ and Cl⁺/H⁺, that show a decrease of 0.8 dex along the diagram as the distance from the bowshock increases. At distances to the bowshock smaller than ~ 4.9 mpc, the abundances of S⁺ and Cl⁺ seem to stabilize and presumably, almost all S and Cl must be only once and twice ionized. This allows the estimation of their total abundances without an ionization correction factor (ICF).

The pixel by pixel distributions of the ionic abundances of Fe and Ni are clearly correlated, as shown in Fig. 11. Similar to that found for S and Cl (see Fig. 10), close to the bowshock, the contribution of species of Fe and Ni with ionic charges higher than Fe²⁺ and Ni²⁺ to their total abundances should be negligible. The ratios of the ionic abundances between both elements remain constant as shown in Fig. 12, being $\log(\text{Fe}^+/\text{Ni}^+) = 1.26 \pm 0.03$, $\log(\text{Fe}^{2+}/\text{Ni}^{2+}) = 1.37 \pm 0.03$ and $\log(\text{Fe}/\text{Ni}) = 1.33 \pm 0.03$. Although the value of $\log(\text{Fe}^{2+}/\text{Ni}^{2+})$ is slightly above the recommended solar value ($\log(\text{Fe}/\text{Ni})_{\odot} = 1.25 \pm 0.05$ (Lodders 2019)), this may be the consequence of a slight systematic underestimation of Ni²⁺ abundance because, as we

discussed in Sec. 4.3, the atomic data for this ion seems to show some inaccuracies.

In Fig. 13 we show the similar pixel by pixel distributions of the He⁺ and Ar²⁺ abundances. Both quantities decrease as we approach the bowshock due to the decrease of the ionization parameter as n_e and the distance from the ionizing star increases. A slight increase is observed at distances less than ~ 2.4 mpc, probably due to the same process discussed in Sec. 5.1 for the case of [O III] lines. However, the impact of this contribution seems to be negligible for these ions. For example, the fact that $T_e(\text{HeI})$ is consistent with $T_e(\text{[N II]})$ (see Sec. 4.1) reflects that the population of the singlet levels, which are the ones used for determining $T_e(\text{HeI})$, are largely unaffected.

In Fig. 14, we show that the abundance of N⁺ increases as we move towards the bowshock from $12 + \log(\text{N}^+/\text{H}^+) = 7.53 \pm 0.03$ to an apparently constant value of 7.75 ± 0.02 . That plateau indicates that all nitrogen should be only once ionized. Figures 15 and 16 show the pixel by pixel distributions of Cr⁺ and Ca⁺ abundances, respectively, which are somewhat different to the ones of Fe⁺ or Ni⁺ (Fig. 11). This makes that the distributions of Fe⁺/Cr⁺ and Fe⁺/Ca⁺ ratios are not constant, contrary to what is obtained for Fe⁺/Ni⁺ (Fig. 17). In the case of the Fe⁺/Cr⁺ ratio, the observed trend may be related to the slight differences between their ionization energies or to different depletion patterns. The curve defined by the Fe⁺/Ca⁺ abundance ratio, may be due to the coexistence of this ion and H⁰ in the ionization front.

What is meant here?
which ionization front?

5.3. A direct measurement of t^2

Several works have studied the possible existence of small spatial scale variations of temperature in the plane of the sky in the Orion Nebula (O'Dell et al. 2003; Mesa-Delgado et al. 2008; García-Díaz et al. 2008). However, the values of the Peimbert's t^2 (Peimbert 1967) estimated in this way may differ substantially from those defined along the line of sight because of the geometry of the Orion Nebula. Fortunately, this does not seem to be a problem in the case of HH 204. Its jet geometry, propagating at an angle of $32 \pm 6^\circ$ with respect to the plane of the sky (See Sec. 8), implies that the integrated volume in the line of sight should be relatively small. If we assume a geometry of an elliptical paraboloid with the UVES slit located in the projection of the symmetry axis in the sky plane (see Fig. 1), then each pixel will integrate the emission of a representative zone of a disc of gas. Variations in the physical conditions would be expected mostly between adjacent discs, being less likely in the azimuthal direction within

Unfortunately, I fundamentally disagree with the premise of this entire t^2 section.
The entire point about the gradients in physical conditions being in the plane of sky applies to the jet bullet, but not at all to the bow shock because it is a curved surface. continued over

The $[O\text{III}]$ is weak from the jet bullet, so there is significant contribution from the bow shock. Therefore, we cannot assume that the variations are predominantly in plane of sky in this case.

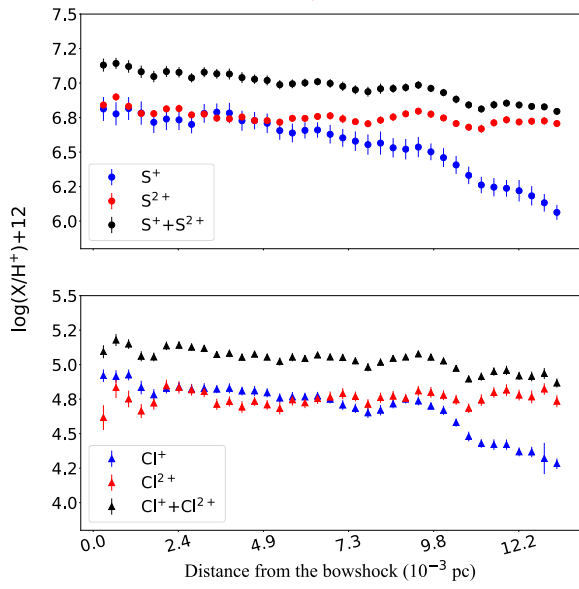


Figure 10: Same as Fig. 6 for ionic abundances of S (upper panel) and Cl (bottom panel).

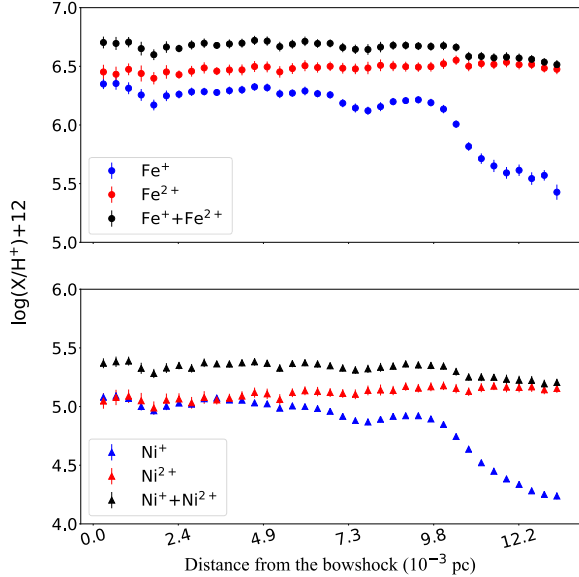


Figure 11: Same as Fig. 6 for ionic abundances of Fe (upper panel) and Ni (bottom panel).

each disc. As discussed in Sec. 5.1, $T_e([O\text{III}])$ shows strong temperature variations along the observed area of HH 204. Since we know the small-scale distribution of the physical conditions and the O^{2+}/H^+ ratio determined using $T_e([O\text{III}])$ along the jet, we can apply the

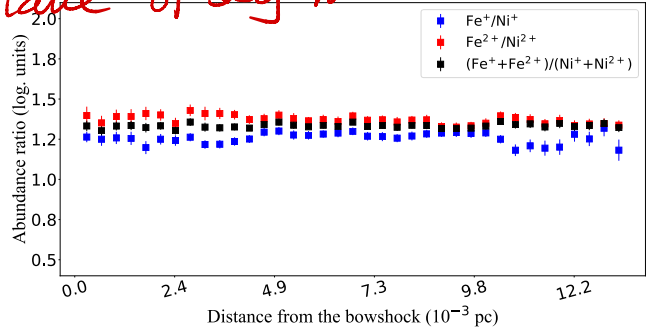


Figure 12: Same as Fig. 6 for the ratios of ionic abundances of Fe and Ni.

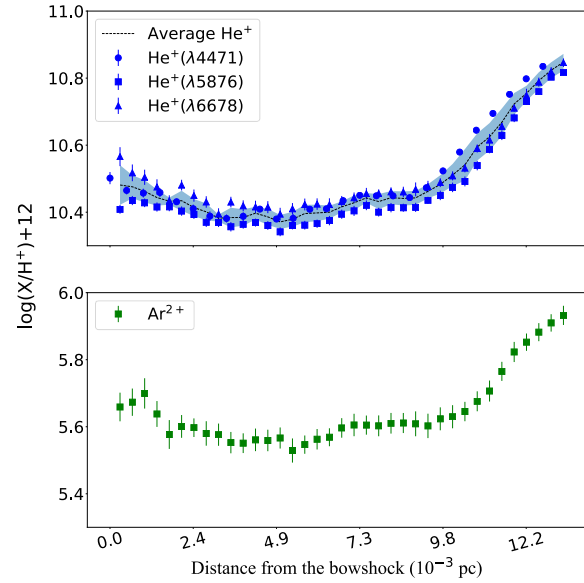


Figure 13: Same as Fig. 6 for He^+ abundances (upper panel) and Ar^{2+} abundances (bottom panel). In the upper panel, the black line indicates the average He^+ abundance obtained with $\text{He I } \lambda\lambda 4471, 5876, 6678$. The color band indicates the associated dispersion.

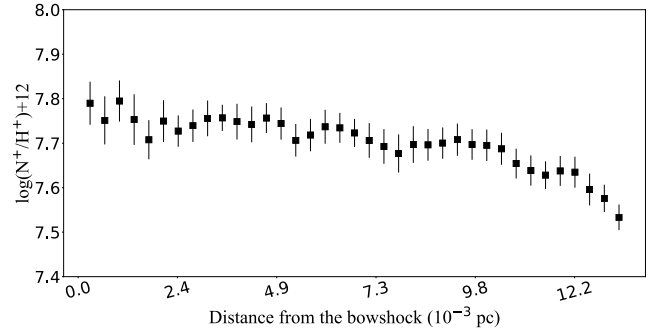


Figure 14: Same as Fig. 6 for N^+ abundances.

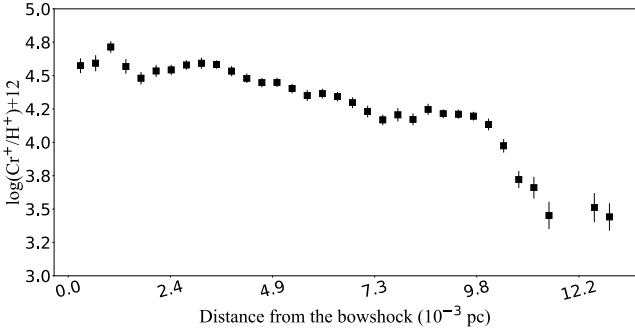


Figure 15: Same as Fig. 6 for Cr⁺ abundances.

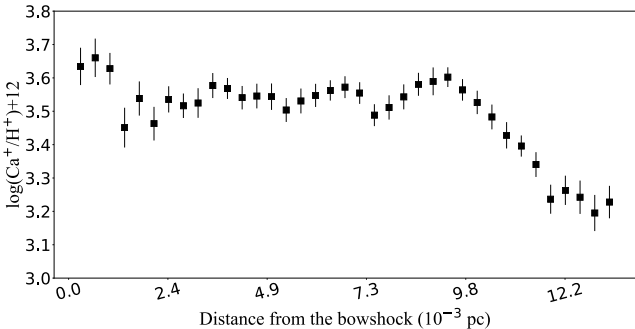


Figure 16: Same as Fig. 6 for Ca⁺ abundances.

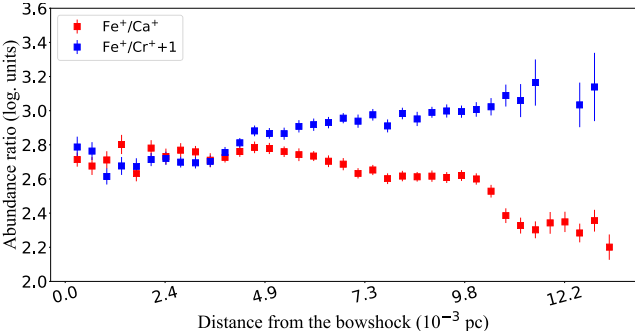


Figure 17: Same as Fig. 6 for Fe⁺/Ca⁺ and Fe⁺/Cr⁺ abundance ratios.

formalism developed by Peimbert (1967) for estimating $t^2(O^{2+})$ and $T_0(O^{2+})$ directly from the definition. Eqs. 9 and 12 from Peimbert (1967), are solved below, by assuming the aforementioned geometry:

$$T_0 = \frac{\int T_e n_e n(O^{2+}) dV}{\int n_e n(O^{2+}) dV} \approx \frac{\sum_{l=0}^{l=d} T_e n_e n(O^{2+}) l^{1/2} \Delta l}{\sum_{l=0}^{l=d} n_e n(O^{2+}) l^{1/2} \Delta l}, \quad (2)$$

$$\begin{aligned} t^2 &= \frac{\int (T_e - T_0)^2 n_e n(O^{2+}) dV}{T_0^2 \int n_e n(O^{2+}) dV} \\ &\approx \frac{\sum_{l=0}^{l=d} (T_e - T_0)^2 n_e n(O^{2+}) l^{1/2} \Delta l}{T_0^2 \sum_{l=0}^{l=d} n_e n(O^{2+}) l^{1/2} \Delta l}, \end{aligned} \quad (3)$$

where l is the distance variable along the jet axis and d is ~ 13 mpc, the maximum observed distance from the bowshock to the edge of the slit. The amplitude of the curvature of the bowshock and the angle of the jet with the plane of the sky are canceled out. The results are $T_0(O^{2+}) = 12040 \pm 80$ K and $t^2(O^{2+}) = 0.012 \pm 0.002$. This is probably the first tentative measurement of t^2 that may be representative for the integrated gas volume of an ionized nebular object. Comparing the results with Eq. 15 from Peimbert (1967), we obtain that the expected $T_e([O\text{ III}])$ we would obtain adding all the pixels considered in the pixel by pixel analysis is 12390 ± 80 K, in agreement with the results of Sec. 4.1 (see Table 3), fact that validates our assumptions. Therefore, in our case, temperature variations of the order of 10^3 K do not break the validity of approximating the temperature-dependence of the emissivity of CELs through the first terms of a Taylor series, and can be properly characterized with Peimbert's t^2 formalism.

5.4. Deuterium lines in HH 204

The emission of deuterium lines in the Orion Nebula was initially recognized by Hébrard et al. (2000a). Unlike the expected isotopic shift of -81.6 km s⁻¹ with respect to the hydrogen lines, they observed a shifted emission around ~ -71 km s⁻¹ from H α and H β . The difference of ~ 10 km s⁻¹ is essentially due to the fact that their emission is produced in different areas of the nebula, where the bulk of gas is moving at different radial velocities. Since the hydrogen lines are produced by recombination in the ionized area that expands towards the observer, the deuterium emission is mainly due to fluorescence excitation with non-ionizing far-UV continuum in areas slightly beyond the ionization front, as the photon dominated region (PDR) or in the H I-H II interface (O'Dell et al. 2001). After the recognition of the deuterium emission in the Orion nebula, this was also identified in other H II regions such as M8, M16, DEM S 103, M20 and S 311 (Hébrard et al. 2000b; García-Rojas et al. 2005, 2006, 2007). As in the Orion Nebula, the deuterium emission in these H II regions has a narrow line width, consistent with their origin in colder areas.

In this work, we detect the emission of D ζ , D ε , D δ , D γ , D β and D α as shown in Fig. 18. In Table 6 we present the characteristics of these emissions. The observed isotopic shift of -81.4 km s⁻¹ between deuterium and hydrogen lines indicates that both kinds of lines arise from HH 204. The observed DI/HI intensity ratios are in good agreement with the predictions of the standard model developed by O'Dell et al. (2001) for the Orion Nebula, confirming the fluorescent nature of